Draft version August 7, 2023
Typeset using LaTeX **twocolumn** style in AASTeX631

Linking the Population of Binary Black Holes with the Stochastic Gravitational-Wave Background

Olivia X. Laske,[1] Patrick M. Meyers,[2] and Arianna Renzini[2]

[1] *Department of Physics and Astronomy, Macalester College, 1600 Grand Av, Saint Paul, MN 55105, USA*
[2] *Division of Physics, California Institute of Technology, 1200 E. California Blvd, Pasadena, CA 91125, USA*

(Dated: 10 July 2023)

Abstract

The astrophysical stochastic gravitational-wave background (SGWB) is the product of overlapping waveforms that create a single unresolvable background. While current LIGO sensitivity is insufficient to uncover the SGWB, future space-based detectors and Third Generation (3G) experiments are expected to probe deep enough for detection. In addition, predictions of the SGWB can still constrain future searches as well as provide insight into star formation, merger history, and mass distribution. Here, two different methods are used to calculate a theoretical SGWB. The first method employs Monte Carlo integration with simulated data, while the second method predefines a grid of mass distributions. After standardizing a prior dictionary across both methods, the output energy density spectra is analyzed with regard to parameters such as binary black hole mass and merger rate. Increasing the maximum merger mass shifts the gravitational-wave (GW) energy density peak to lower frequencies, while increasing the local merger rate proportionally affects the GW energy density.

1. INTRODUCTION

Gravitational-waves (GWs), which present as perturbations in spacetime, are the product of large scale, highly energetic events. GWs were first observed in 2015 by the Laser Interferometer Gravitational-Wave Observatory (LIGO), located in Livingston, Louisiana and Hanford, Washington, with the detection of GW150914, a binary black hole merger (Abbott et al. 2016). LIGO is joined by several other ground-based GW observatories, including Virgo in Italy, GEO600 in Germany, and KAGRA (Kamioka Gravitational-Wave Detector) in Japan. In addition, the space-based detector Laser Interferometer Space Antenna (LISA) and Third Generation (3G) experiments Einstein Telescope (ET) and Cosmic Explorer (CE) are expected to launch in the 2030s.

LIGO takes the form of a Michelson interferometer, in which an incident laser beam is split into orthogonal reflected and transmitted beam components along the two arms of the detector. The beams are subsequently reflected back toward the beam splitter and recombined. During a GW event, the arms of the detector are compressed and rarefied, causing the two beams to shift out of phase and form a detectable interference pattern.

LIGO relies on cross correlation to confirm GW signals. The numerous noise sources, ranging from the seismic noise of ocean waves and earthquakes to the thermal noise of suspension mirror resonance frequencies, prove difficult to distinguish from GW signals, especially as the strain produced by GWs are on the order of 10^{-21} m (Abbott et al. 2016). As a result, ensuring that the signal appears at multiple interferometers both reliably confirms GW signals and allows for more accurate sky localization.

GW signals are often categorized into continuous, compact binary inspiral, burst, and stochastic types. Continuous GWs are produced by large, rotating systems, such as neutron stars, and appear as a sinusoidal pattern of detector strain over long periods of time (Piccinni 2022). Compact binary inspirals arise from mergers of dense objects, such as black hole and neutron star

olaske@macalester.edu
pmeyers@caltech.edu
arenzini@caltech.edu

mergers, and are characterized by a chirp signal in time-frequency space (Bustillo et al. 2020). Through O3, LIGO has detected 90 GW events stemming from compact binary inspirals (Piccinni 2022). Burst GW sources include Type II supernovae and are measured on short time scales (Abbott et al. 2019). Finally, stochastic signals are the sum of numerous unresolved GW sources that form a GW background. LIGO has yet to detect continuous GW, burst, and stochastic signals.

2. THE STOCHASTIC GRAVITATIONAL WAVE BACKGROUND

The stochastic gravitational-wave background (SGWB) is of particular interest, especially as the involved GWs can originate from the very early Universe, not long after the Big Bang. Because the Universe at the time was opaque to photons, the SGWB is one of the only means of studying this era. In addition, understanding the effect of binary black hole population on the SGWB constrains properties such as merger rate and mass distribution.

The SGWB is often divided into two categories: cosmological and astrophysical. Cosmological sources include events that occurred in the early Universe, such as inflation. In the case of inflation, rapid expansion drove the GWs at the time into an isotropic background. Astrophysical sources are comprised of individual events such as mergers and pulsars. Figure 1 depicts the predicted SGWBs for several cosmological and astrophysical sources across the frequency spectrum. Each

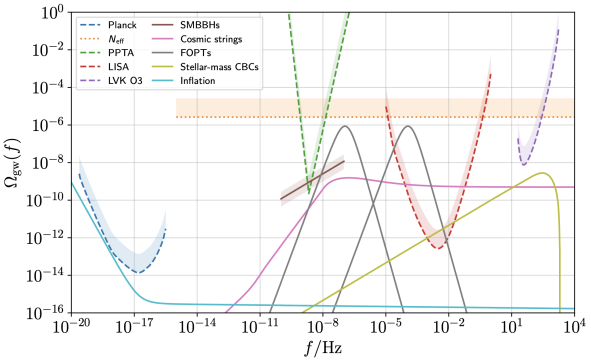

Figure 1. Predicted GW backgrounds from different sources across the frequency spectrum. Figure from (Renzini et al. 2022).

color represents a different source of GWs. The project specifically focuses on the frequency sensitivity of LIGO, 10 Hz to 10 kHz (Martynov et al. 2016), which corresponds to the very upper range of Figure 1. The brown line represents the predicted background due to supermassive binary black holes (SMBBH). The project also investigates stellar mass binary black holes, which are expected to be the majority of the BBH signal in the LIGO frequency range. The predicted SMBBH signal lies in the 10^{-10} Hz to 10^{-7} Hz range, which is outside of LIGO sensitivity of approximately 1 to 100 $M_\odot$ black holes, suggesting that BBHs between 10 Hz and 10 kHz are not supermassive.

Detector sensitivity and resolution limits cause these sources to appear unresolved, the signals of which then overlap to create a measurable SGWB. With current detector sensitivity, though, the SGWB is undetectable, as illustrated in Figure 2.

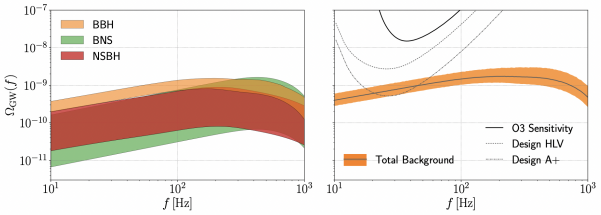

Figure 2. Current detector limits with regard to the SGWB. Figure from (Renzini et al. 2022).

In addition, detectors must be sufficiently far apart in order to ensure that they are not receiving identical noise sources. One consequence of physically distant detectors, though, is the overlap reduction function, shown for LIGO Hanford and LIGO Livingston in Figure 3. An oscillating GW signal is time-shifted between the detectors, which reduces signal correlation between them. As a result, assuming an isotropic, Gaussian SGWB, LIGO is more sensitive to low-frequencies, where the wavelength is much greater than the distance between the detectors.

However, design A+ LIGO as well as detectors LISA, ET, and CE will begin to probe the sensitivities required to detect the SGWB from unresolved compact binary mergers.

3. METHODS

Several different methods may be used to calculate the SGWB. The first method, developed by Thomas Callister (hereby referred to as the Callister method), uses a predefined mass distribution to create a grid of either (m_1, m_2) or (m_1, q) points, convert them to $(\ln M_{\rm tot}, q)$ space with the Jacobian, and calculate the spectral energy density at each grid point. The second method, devloped in C by Tania Regimbau and rewritten in Python

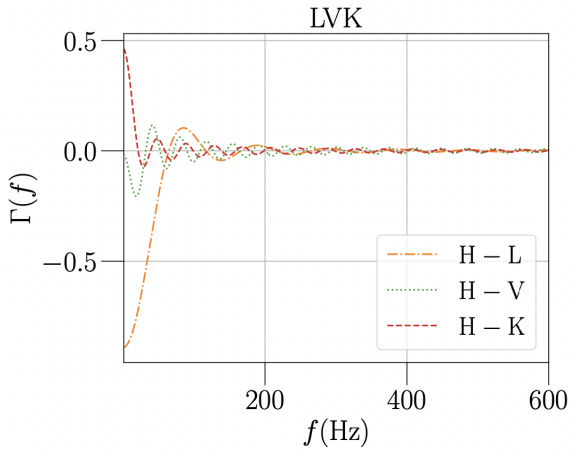

Figure 3. Overlap reduction function for the LVK network. Figure from (Renzini et al. 2022).

by Arianna Renzini (the Regimbau method), generates a frequency domain waveform and calculates the power spectral density for each injection in a list of injections. The third method (combined method) combines the previous two methods and uses a list of injections to define a mass distribution.

3.1. *Theoretical Calculation of the SGWB*

The SGWB is typically modeled by a power law of the following form:

$$\Omega_{\rm GW}(f) = \Omega_{GW}(f_{\rm ref}) \left(\frac{f}{f_{\rm ref}}\right)^{\alpha}, \tag{1}$$

where $\Omega_{\rm GW}(f)$ is dimensionless GW energy density, f is frequency, and α is the spectral index of the signal. The GW energy density can be decomposed as follows:

$$\Omega_{\rm GW}(f) = \frac{1}{\rho_{\rm c}} \int_0^{\infty} dz \frac{N(z)}{1+z} \left[f_{\rm r} \frac{dE_{\rm GW}}{df_{\rm r}} \right]_{f_{\rm r}=f(1+z)}, \tag{2}$$

$$\rho_{\rm c} = \frac{3H_0^2}{8\pi G}, \tag{3}$$

where ρ_c is critical density, $\dot{N}(z)$ is number of GW sources as a function of redshift, z is redshift, $dE_{\rm GW}/df_r$ is spectral energy density, f_r is rest frame frequency, $H_0 = 67.4$ km s^{-1} Mpc^{-1} is the Hubble constant (see Appendix A), and $G = 6.6743015 \cdot 10^{-11}$ m^3 kg^{-1} s^{-2} is the universal gravitational constant. The integral of Equation 2 encompasses the entirety of the Universe's history. The components inside the integral multiply $N(z)$ by the spectral energy density weighted by f. At $z = 0$, $f_r = f$, and $\Omega_{\rm GW}(f) = f(N_0/\rho_{\rm c})(dE_{\rm GW}/df)$. As a result, $\Omega_{\rm GW}$ is proportional to $N(z)$.

Fractional energy density can be averaged over source parameters θ. In addition, $N(z)$ can be rewritten in terms of event rate, redshift and the Hubble parameter. Therefore, Equation 2 becomes the following after removing f from the integral:

$$\Omega_{\rm GW} = \frac{f}{\rho_{\rm c}} \int_0^{z_{\rm max}} dz \frac{\dot{N}(z)}{(1+z)H(z)} \left\langle \frac{dE_{\rm GW}}{df_{\rm r}}\bigg|_{f_{\rm r}=f(1+z)} \right\rangle, \tag{4}$$

$$\left\langle \frac{dE_{\rm GW}}{df_{\rm r}} \right\rangle = \int d\theta p(\theta) \frac{dE_{\rm GW}(\theta; f_{\rm r})}{df_{\rm r}}, \tag{5}$$

where $H(z)$ is the Hubble parameter as a function of redshift (see Appendix A).

3.2. *Calculation of the SGWB with the Callister Method*

The Callister method takes form in four distinct steps:

1. Define the local merger rate.
2. Calculate the merger rate.
3. Determine the mass distribution probability grid.
4. Calculate the GW energy density $\Omega_{\rm GW}$.

The steps are described in the following sections.

3.2.1. *Definition of the Local Merger Rate*

The local merger rate describes the merger rate, which is the total number of mergers that occur per cubic Gpc per year, at $z = 0$. A BBH local merger rate is defined for subsequent merger rate density normalization. The Callister method uses $R_0 = 28.3$ Gpc^3 yr^{-1}, the Power Law + Peak BBH merger rate ($z = 0.2$) from Abbott et al. (2022).

3.2.2. *Calculation of the Merger Rate*

The merger rate is often modelled as follows:

$$\dot{N}(z) = \mathcal{C}(\alpha, \beta, z_{\rm p}) \frac{\dot{N}_0 (1+z)^{\alpha}}{1 + (\frac{1+z}{1+z_{\rm p}})^{\alpha+\beta}}, \tag{6}$$

$$\mathcal{C}(\alpha, \beta, z_{\rm p}) = 1 + (1+z_{\rm p})^{-(\alpha+\beta)}, \tag{7}$$

where $\dot{N}_0$ is the current merger rate and $\mathcal{C}(\alpha, \beta, z_{\rm p})$ is a normalization constant to satisfy the boundary condition $\dot{N}(0) = \dot{N}_0$. Values α and β shape the growth and decay of $\dot{N}(z)$ before and after peak redshift $z_{\rm p}$. Figure 4 displays a plot of the merger rate as a function of redshift.

Redshift bins are set from $z = 0$ to $z = 10$ such that $dz = 0.01$, and the merger rate is calculated for each redshift bin using $\alpha = 1.9$, $\beta = 3.4$, and $z_{\rm p} = 2.4$.

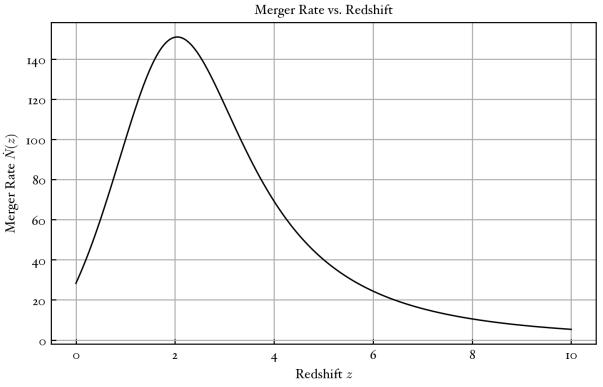

Figure 4. Merger rate using $\alpha = 1.9$, $\beta = 3.4$, $z_{\rm p} = 2.4$, and $\dot{N}_0 = 31.88$ Gpc^{-3} yr^{-1}.

3.2.3. *Determination of the Mass Distribution Probability Grid*

The minimum and maximum BH masses are set such that $m_{\rm min} = 5$ M$_\odot$ and $m_{\rm max} = 50$ M$_\odot$. A probability grid of the mass distribution is defined in (m_1, q) space using `prior.prob` on `bilby` priors. The probabilities are then converted to $(\ln M_{\rm tot}, q)$ space with the Jacobian and normalized. Callister (2021) provides a table of Jacobians that converts between mass parameter pairs.

$$\frac{dP}{d\ln M_{\rm tot} dq} = \frac{dP}{dm_1 dq}\frac{M_{\rm tot}}{(1+q)}. \tag{8}$$

3.2.4. *Calculation of the GW Energy Density*

Once the mass distribution probability grid has been determined, the GW energy density can be calculated.

For inspiralling compact binary systems, the spectral energy density $dE_{\rm GW}/df_{\rm r}$ is determined by the following:

$$\frac{dE_{\rm GW}}{df} = \frac{(G\pi)^{2/3}\mathcal{M}^{5/3}}{3} H(f), \tag{9}$$

$$\mathcal{M} = \frac{(m_1 m_2)^{3/5}}{(m_1+m_2)^{1/5}}, \tag{10}$$

$$H(f) = \begin{cases} f^{-1/3} & (f < f_{\rm merge}) \\ \frac{f^{2/3}}{f_{\rm merge}} & (f_{\rm merge} \leq f < f_{\rm ring}) \\ \frac{1}{f_{\rm merge} f_{\rm ring}^{4/3}} \left(\frac{f}{1+(\frac{f-f_{\rm ring}}{\sigma/2})^2} \right)^2 & (f_{\rm ring} \leq f < f_{\rm cutoff}) \\ 0 & (f \geq f_{\rm cutoff}) \end{cases}. \tag{11}$$

Here, $\mathcal{M}$ is chirp mass, m_1 and m_2 are component masses, f is frequency, $f_{\rm merge}$ is the merger frequency, $f_{\rm ring}$ is the ringdown frequency, $f_{\rm cutoff}$ is the cutoff frequency, and σ is the width of the Lorentzian function around $f_{\rm ring}$ (Callister et al. 2016). Parameters $f_{\rm merge}$, $f_{\rm ring}$, $f_{\rm cutoff}$, and σ are given by Table I in Ajith et al. (2008).

Probability $p(\theta)$ in Equation 5 is given for (m_1, m_2) by the mass distribution probability grid, and $\mathcal{M}$ is calculated from m_1 and m_2. The merger rates and average spectral energy density are then inserted into Equation 4 to obtain the final GW energy density. Note that the Callister method approximates the Hubble rate and does not include the $\Omega_{\rm R}$ and $\Omega_{\rm k}$ terms.

3.3. *Calculation of the SGWB with the Regimbau Method*

The Regimbau method begins by setting `bilby` priors, outlined in Table 1.

Prior	Distribution	Parameters
mass_1	Power Law	$\alpha = -2.3$
mass_ratio	Power Law	$\alpha = 1.5$
chi_1	0	0
chi_2	0	0
theta_jn	Uniform	min = 0, max = 2π
geocent_time	Uniform	min = 0, max = T_obs

Table 1. Prior distributions used in the Regimbau method.

In addition to `bilby` priors, a new redshift prior is defined by the following equation:

$$p(z) = \frac{1}{1+z}\dot{N}(z)\frac{dV_{\rm c}}{dz}(z), \tag{12}$$

where $\dot{N}(z)$ is defined as in Equation 6. $dV_{\rm c}(z)/dz$ is defined as follows:

$$\frac{dV_{\rm c}}{dz}(z) = \frac{4\pi c d_{\rm c}(z)^2}{H(z)}, \tag{13}$$

$$d_{\rm c}(z) = \int_0^z \frac{c}{H(z)} dz, \tag{14}$$

$$\tag{15}$$

where $dV_{\rm c}(z)/dz$ is the comoving volume per unit redshift, $c = 2.998 \cdot 10^8$ m s^{-1} is the speed of light, and $d_{\rm c}(z)$ is the comoving distance as a function of redshift.

The priors are then sampled using `bilby`. The resulting injections are inserted into the `Simulator` module of Python library `pygwb` (Python-based library for gravitational-wave background-searches), which calculates $\Omega_{\rm GW}$ by summing the spectral energy density of

each event (Renzini et al. 2023):

$$\frac{dE}{df} = |h_+|^2 + |h_\times|^2, \tag{16}$$

where h_+ is the plus polarization and $h_\times$ is the cross polarization. The GW energy density is then calculated with the following equation:

$$\Omega_{\rm GW}(f) = \frac{2}{T_{\rm obs}} \sum_0^N \frac{2\pi^2 f^3}{3H_0^2} \frac{dE}{df}, \tag{17}$$

where $T_{\rm obs}$ is the observation time and N is the number of sampled events. N is given by Callister et al. (2020):

$$N(\alpha, \beta, z_{\rm p}, \dot{N}_0) = T_{\rm obs} \int_0^{z_{\rm max}} dz \frac{1}{1+z} \dot{N}(\alpha, \beta, z_{\rm p}, \dot{N}_0; z) \frac{dV_{\rm c}}{dz}. \tag{18}$$

After computing a theoretical value for N, the number of injections is determined with a Poisson process (see Appendix B).

In order to increase the observing time while keeping a reasonable run time, $\Omega_{\rm GW}$ averaged over n iterations. The number of injections in each iteration still uses a Poisson process.

3.4. *Combined Calculation of the SGWB*

The combined method establishes the same `bilby` priors as the Regimbau method and uses Equation 18 with a Poisson process to determine the number of samples. The merger rate is calculated with Equation 6, and $dV_{\rm c}/dz$ is calculated with Equation 13.

The component masses are calculated from m_1 and q. Equation 10 can be used to find the chirp masses, which are then inserted into Equation 9. Equations 5, 9, and 11 are used to determine the final GW energy density spectrum. As in the Callister method, parameters $f_{\rm merge}$, $f_{\rm ring}$, $f_{\rm cutoff}$, and σ are taken from Ajith et al. (2008).

4. RESULTS

While modifications to each of the methods are still in progress, the following figures display preliminary results. Figure 5 is of the final GW energy density spectrum obtained from the Callister method.

Figure 6 displays the spectrum using the Regimbau method with an observation time of 1 day. We plan to investigate the peak at higher frequencies in the Regimbau plot that appears regardless of the observation time. We also plan to look into the deviation of the Regimbau plot from the 2/3 power law at higher frequencies.

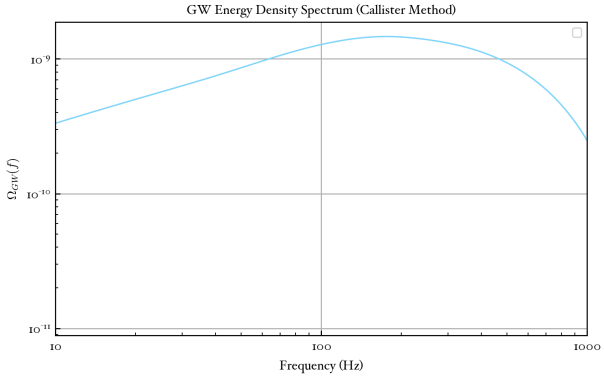

Figure 5. GW energy density spectrum generated from the Callister method.

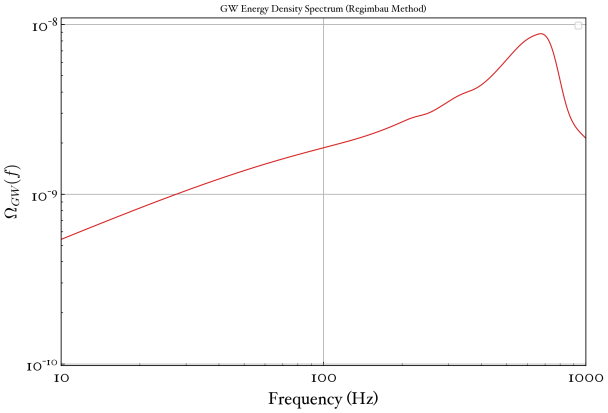

Figure 6. GW energy density spectrum generated from the Regimbau method.

Figure 7 plots Figures 5 and 6 on the same graph for comparison. The Callister method produces a lower GW energy density spectrum than the Regimbau method. At lower frequencies, both methods show relative consistency, though they begin to deviate at higher frequencies.

Figure 8 displays the spectrum from the combined method with an observation time of 1 day. While the combined method is still in progress, preliminary results show that the GW energy density is approximately an order of magnitude too low.

Figure 9 demonstrates a comparison of the GW energy density spectrum with three different local merger rates. The green curve is the BBH merger rate from the Power Law + Peak model in Abbott et al. (2022). The red and blue curves are the lower and upper bounds, respectively, of the merger rate. Note that the merger rates in Abbott et al. (2022) are given with $z = 0.2$.

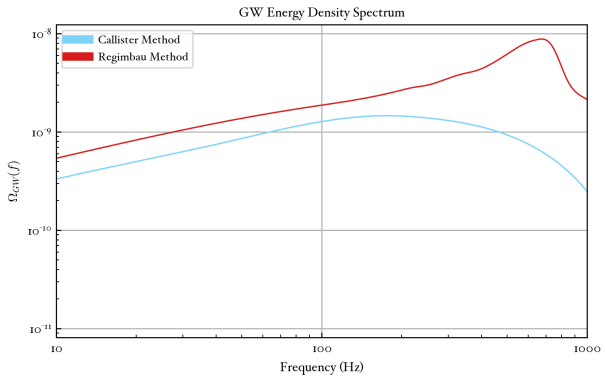

Figure 7. GW energy density spectrum comparison of the Callister method to the Regimbau method.

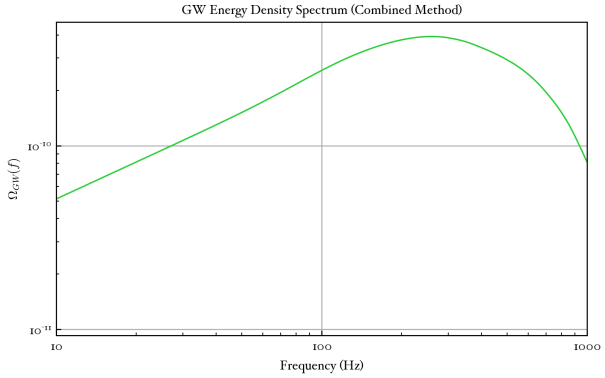

Figure 8. GW energy density spectrum generated from the combined method.

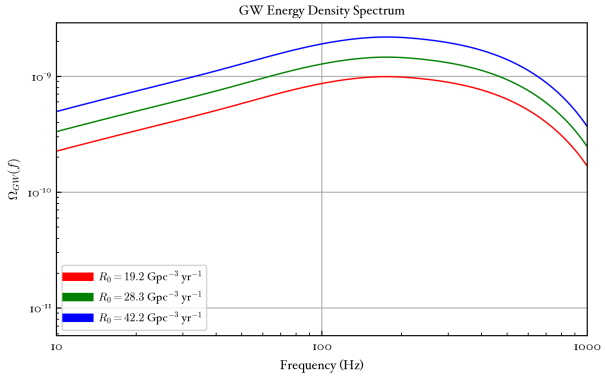

Figure 9. GW energy density spectrum with varying merger rates.

Finally, Figure 10 displays the GW energy density spectrum produced by varying maximum black hole masses. The middle curve is the maximum mass of a black hole from Abbott et al. (2022), with the first and fifth curves representing the lower and upper limits. From plots of the GW energy density peak (see Figure 11), a clear trend emerges. As the maximum merger mass increases, the peak frequency decreases.

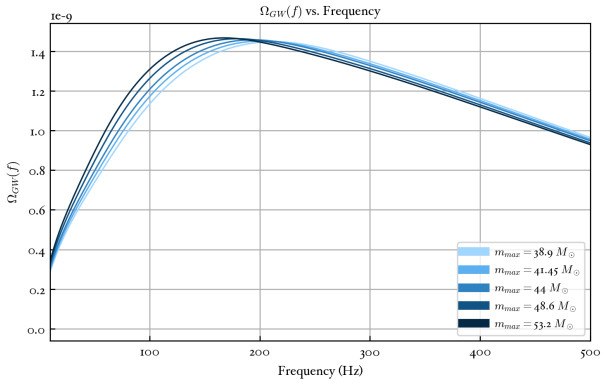

Figure 10. GW energy density spectrum with varying maximum merger masses.

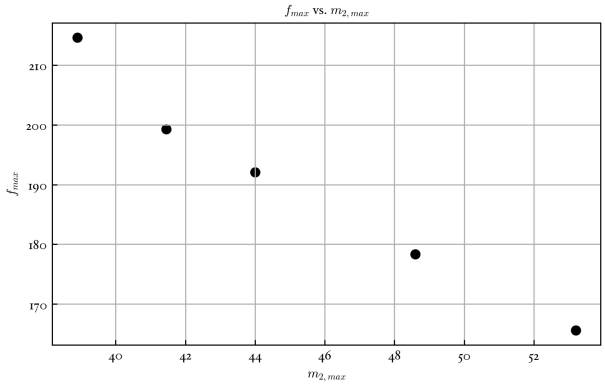

Figure 11. GW energy density peak frequencies with varying maximum merger masses.

5. ACKNOWLEDGEMENTS

This material is based upon work supported by the National Science Foundation. Any opinions, findings, and conclusions or recommendations expressed in this material are those of the author(s) and do not necessarily reflect the views of the National Science Foundation.

I would like to thank my mentors, Patrick Meyers and Arianna Renzini, and LIGO SURF program director, Alan Weinstein, for their support and guidance. I would also like to thank Tania Regimbau and Thomas Callister for their code.

REFERENCES

Abbott, B. P., Abbott R., Abbott, T. D., et al. 2016, Phys. Rev. Lett., 116, 061102

Abbott, B. P., Abbott R., Abbott, T. D., et al. 2019, Astrophys. J., 886, 75

Abbott, R., Abbott, T. D., Acernese, F., et al. 2022, Phys. Rev. X, 13, 011048

Aghanim, N., Akrami, Y., Ashdown, M., et al. 2020, A&A, 641, A6

Ajith, P., Babak, S., Chen, Y., et al. 2008, Phys. Rev., D 79, 104017

Bustillo, J. C., Evans, C., Clark, J. A., et al. 2020, Commun. Phys., 3, 176

Callister, T., Letizia, S., Shi, Q., et al. 2016, Phys. Rev., 6, 3

Callister, T., Fishbach, M., Holz, D. E., & Farr, W. M. 2020, ApJL, 896, L32

Callister, T. 2021, arXiv:2104.09508v1 [gr-qc]

Martynov, D. V., Hall, E. D., Abbott., B. P., et al. 2016, Phys. Rev., D 93, 112004

Piccinni, O. J. 2022, Galaxies, 10(3), 72

Renzini, A. I., Goncharov, B., Jenkins, A. C., & Meyers, P. M. 2022, Galaxies, 10, 0

Renzini, A. I., Romero-Rodriguez, A., Talbot, C., et al. 2023, AAS

Vangioni, E., Goriely, S., Daigne, F., et al. 2016, MNRAS, 455, 17

APPENDIX

A. HUBBLE RATE

The Hubble parameter is a measure of the expansion of the universe in km s^{-1} Mpc^{-1}.

$$H(z) = H_0(\Omega_{\rm R}(1+z)^4 + \Omega_{\rm M}(1+z)^3 + \Omega_{\rm k}(1+z)^2 + \Omega_\Lambda)^{1/2}, \tag{A1}$$

$$\Omega_{\rm R} = \Omega_\gamma + \Omega_\nu + \Omega_{\rm GW} + ..., \tag{A2}$$

where $H(z)$ is the Hubble parameter, H_0 is the current Hubble parameter, z is redshift, and Ω is the energy density with R as the radiation component, M as the matter component, k as the curvature, and Λ as the cosmological constant, representative of dark energy. R is composed of photons, neutrinos, and GWs. M is composed of baryons and cold dark matter. According to the Planck 2018 cosmological parameters, $H_0 = 67.66 \pm 0.42$ km s^{-1} Mpc^{-1}, $\Omega_{\rm R} = 9.182 \times 10^{-5}$, $\Omega_{\rm M} = 0.3111 \pm 0.0056$, $\Omega_{\rm k} = 0.001 \pm 0.002$, and $\Omega_\Lambda = 0.6889 \pm 0.0056$ (Aghanim et al. 2020).

The quantity $\Omega_{\rm R}$ is particularly notable at high redshift, which is concurrent with the radiation-dominated era of the cosmological timeline, suggesting that $\Omega_{\rm GW}$ becomes a measurable quantity when probing the early Universe.

B. POISSON PROCESS

A Poisson process is a method used for weighted sampling and is defined by the following equation:

$$p(n) = \frac{(\lambda t)^n}{n!} e^{-\lambda t}. \tag{B1}$$

In the context of the SGWB, p is the probability that n events occurs in an observing time t and λ is the total merger rate. Therefore, λt is equivalent to N in Equation 18. Equation B1 then represents a probability distribution from which to draw the number of injections.